Supplementary Information

An artificial leaf device built with earth-abundant materials for combined H_2 production and storage as formate with efficiency > 10%

Claudio Ampelli,*[a] Daniele Giusi,[a] Matteo Miceli,[a] Tsvetelina Merdzhanova,[b] Vladimir Smirnov,[b] Ugochi Chime,[b] Oleksandr Astakhov,[b] Antonio José Martín,[c] Florentine Louise Petronella Veenstra,[c] Felipe Andrés Garcés Pineda,[d] Jesús González-Cobos,[d†] Miguel García-Tecedor,[e‡] Sixto Giménez,[e] Wolfram Jaegermann,[f] Gabriele Centi,[a] Javier Pérez-Ramírez,[c] José Ramón Galán-Mascarós,[d] and Siglinda Perathoner[a]

[a.] *Department of Chemical, Biological, Pharmaceutical and Environmental Sciences (ChiBioFarAm), University of Messina, ERIC aisbl and CASPE/INSTM; Messina, Italy.* **E-mail: ampellic@unime.it*
[b.] *IEK5-Photovoltaik, Forschungszentrum Jülich GmbH, 52425 Jülich, Germany*
[c.] *Institute for Chemical and Bioengineering, Department of Chemistry and Applied Biosciences, ETH Zürich, Vladimir-Prelog-Weg 1, 8093 Zürich, Switzerland*
[d.] *Institute of Chemical Research of Catalonia (ICIQ), The Barcelona Institute of Science and Technology (BIST), Av. Paisos Catalans 16, 43007 Tarragona, Spain*
[e.] *Institute of Advanced Materials (INAM), Universitat Jaume I; Castelló, Spain*
[f.] *Technical University of Darmstadt, 64287 Darmstadt, Germany*

[†] *Present Address: Institut de Recherches sur la Catalyse et l'Environnement de Lyon, UMR 5256, CNRS, Université Claude Bernard Lyon 1, 2 Avenue A. Einstein, 69626 Villeurbanne, France*
[‡] *Present Address: Photoactivated Processes Unit, IMDEA Energy, Avda. Ramón de la Sagra, 3, 28935 Móstoles, Spain*

S1. Electrolyte and pH

Figure S1 shows the potential/pH diagram (Pourbaix diagram) for Cu, S, and O species in an aqueous medium, outlining the possible phases of the electrocatalyst in equilibrium during CO_2 reduction. The explored pH areas for both cathode and anode are pretty limited (as shown by the blue and red regions of the diagram). For the anode part, a pH lower than 11 affects the Ni-based anode's performance and stability in OER; thus, we used KOH 1 M without flowing CO_2 into the anode part. Moreover, pH and electrolyte concentration are two interdependent parameters in the cathode part. It is impossible to increase the pH above 8.1, which refers to a $KHCO_3$-saturated solution in water (3.6 M), saturated with CO_2 at 1 atm.

Therefore, to maximise the performances of the Cu-based electrocatalyst in the cathode for CO_2 reduction and the Ni-based catalyst in the anode for OER, **the operating set pH values must be different in the two half-cells**. Using a PTFE-reinforced Nafion® membrane may help maintain the pH difference in the compartments, as proved by the experimental tests, at least in the period time of the experiments (< 10 hours).

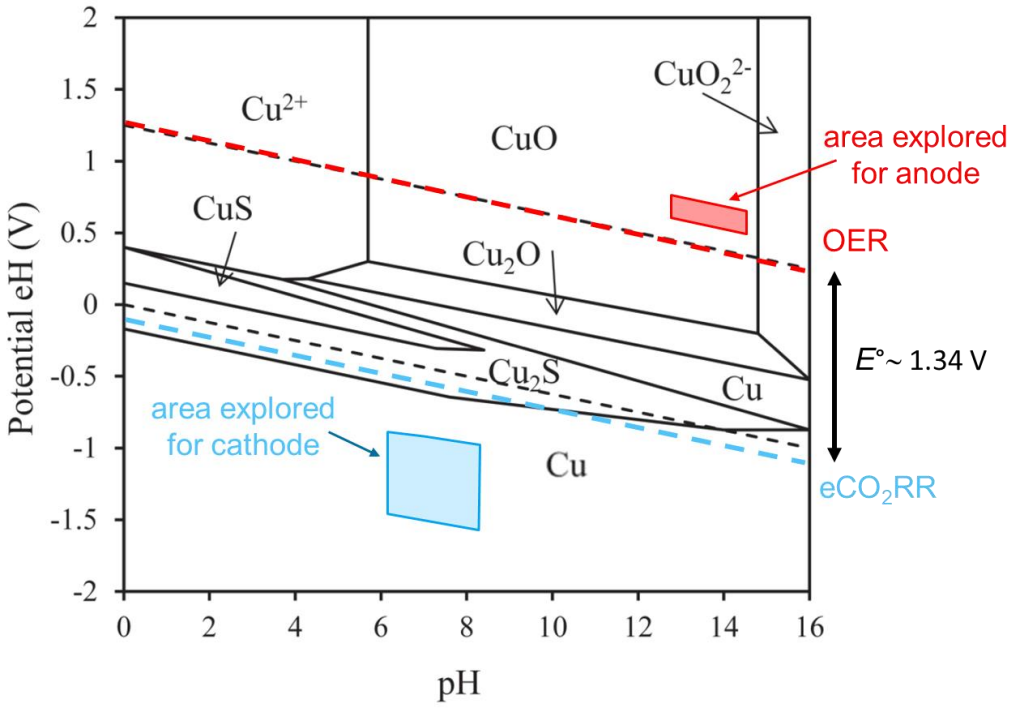

Figure S1. *Pourbaix diagram (Potential vs. pH) for Cu, S, and O species in aqueous medium and indication of thermodynamic equilibrium potentials for the oxygen evolution reaction (OER) and CO_2 electroreduction (eCO_2RR) (dashed). Coloured areas correspond to explored conditions during preliminary tests.*

S2. Optimal catholyte pH

The Cu-S electrocatalyst was preliminarily tested at different catholyte pH, using a cathodic potential of -0.8 V vs RHE. Specifically, these tests were performed at pH 5.9, 6.8 and 8.1 by saturating with CO_2 three solutions of $KHCO_3$ 0.01, 0.1 and 8.1 M, respectively.

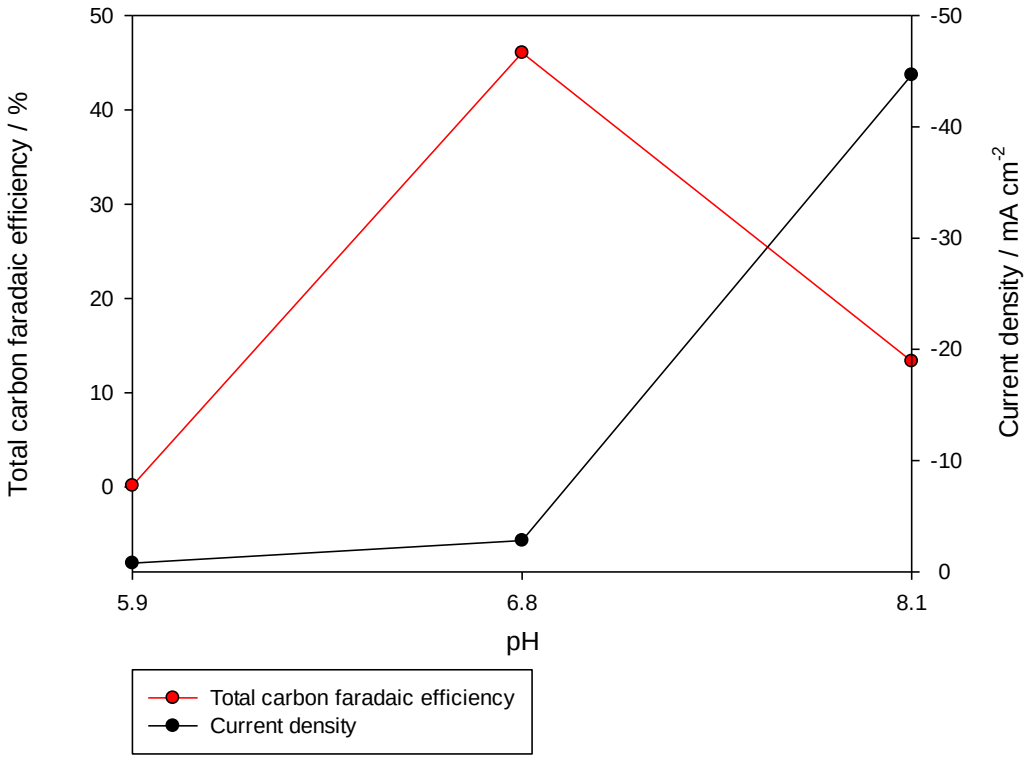

Figure S2. Current density and total carbon FE % profiles at different pH, under -0.8 V vs. RHE applied voltage.

The current density increases with the pH, as expected due to the increase in $KHCO_3$ concentration, reaching current density values of about 45 mA cm^{-2} at pH=8.1. However, the best performances in terms of carbon products (formate and carbon monoxide) were obtained at pH=6.8 (see Figure S2).

S3. Selection of the best exchange membrane

We investigated the electrochemical behaviour of multiple commercially available membranes of different types (cationic, anionic and bipolar). Tests were made using a standard H-type cell (the most commonly reported in the literature) and a three-electrode flow cell using 0.1 M $KHCO_3$ as catholyte and 1 M KOH as anolyte. Table S1 reports the list of membranes investigated and their overall resistances measured in the two cells. Note that the resistance values measured in the H-type cell are affected by a significant error in the case of bicarbonate, due to the difficulty of positioning accurately the electrodes (a difference of only 1 mm in the electrode distance corresponds to about 5 Ω). However, the cell resistance values measured in the compact lab-scale cell are very accurate.

Table S1: *List of different exchange membranes investigated and overall cell resistances measured in H-type and compact flow cells.*

			H-type cell		compact flow cell
	Membrane	Thickness (µm)	R in 0.1M $KHCO_3$ ± 4.8 (Ω)	R in 1M KOH ± 0.1 (Ω)	R in 0.1M $KHCO_3$ and 1M KOH ± 0.1 (Ω)
	No Membrane	-	48.0 Ω/cm	0.7 Ω/cm	-
CATION	Nafion HP	20	16.0	5.4	15.5
CATION	Nafion NR 212	50.8	7.0	12.9	15.3
CATION	Nafion N 115	127	17.0	16.2	17.7
CATION	Nafion N 117	183	19.0	18.7	17.2
CATION	Nafion N324 *(reinforced)*	280	18.5	*not stable – destroyed**	21.3
CATION	Nafion N424 *(reinforced)*	380	16.5	*not stable – destroyed**	22.0
ANION	Fumapem-3-30	*low*	8.0	0.1	*not stable – osmosis**
ANION	Sustainion X 37-50	*low*	10.0	0.1	*not stable – osmosis**
ANION	Fumapem FAA-3-PE-20	*low*	-	-	*not stable – osmosis**
ANION	FAA-3-05-RF	*low*	-	-	*not stable – osmosis**
ANION	Fumasep FAA-3-PK-75 *(reinforced)*		-	-	17.1
BIPOLAR	Fumasep FBM-PK	130-160	26.0	2.0	18.9

not stable – destroyed: Teflon-side of the membrane (cathode side) not stable in 1M KOH*

not stable – osmosis: problems of water migration from cathode to anode observed in 30 min*

In the case of the anionic exchange membranes (they are very thin membranes), we observed an evident osmosis phenomenon from catholyte to anolyte (we noticed a change in the liquid level in the two reservoirs) due to the different salt concentrations between anode and cathode. As a result, we could determine the cell resistance (17.1 Ω) only for the reinforced one (Fumasep FAA-3-PK-75). However, osmosis was also observed for longer times (> 2 hours). Regarding the Nafion

membranes, we found that the resistance values of the PTFE-reinforced membranes were higher with respect to not-reinforced ones; however, they enormously helped to limit the crossover of products (i.e., formate from the cathode to anode). Moreover, the thinner Nafion membranes also showed osmosis phenomena for longer times. Thus, we selected the N324 Nafion reinforced membrane (21.3 Ω of resistance) and the bipolar Fumasep FBM-PK membrane (18.9 Ω) as candidates for further investigations. In particular, we analysed the two membranes by chronopotentiometry at 10 mA cm^{-2}. The results, reported in Figure S3, evidenced good cell resistance and pH stability for both the selected membranes.

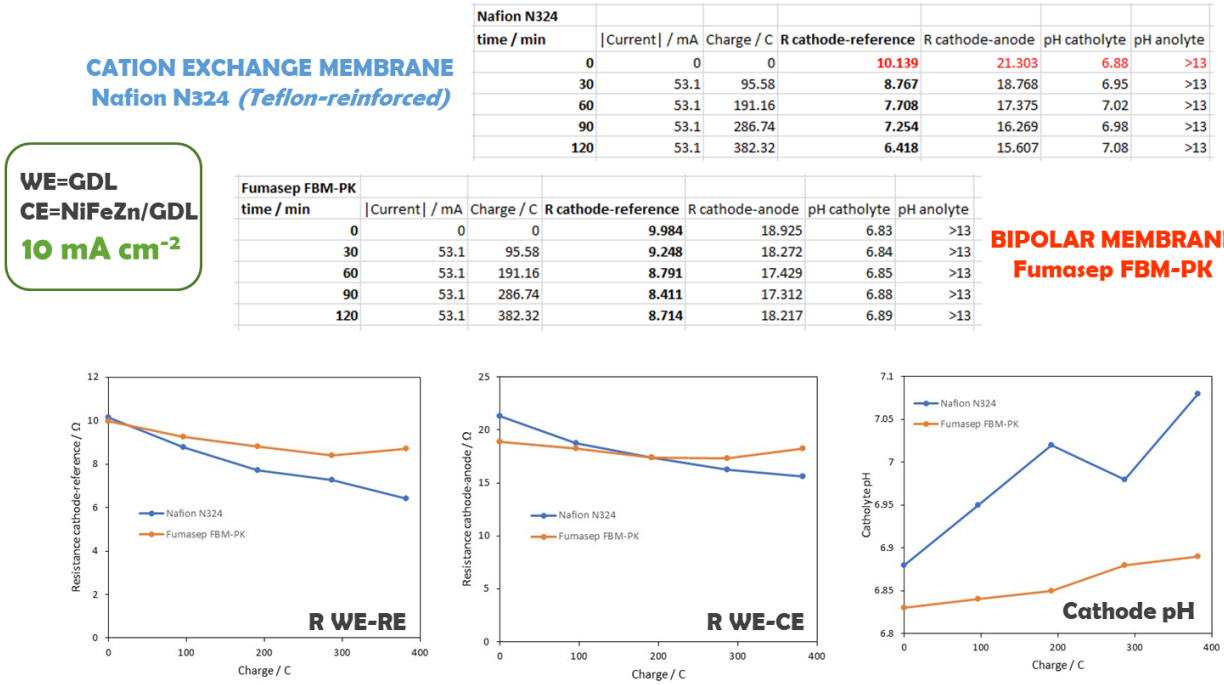

Nafion N324

time / min	|Current| / mA	Charge / C	R cathode-reference	R cathode-anode	pH catholyte	pH anolyte
0	0	0	10.139	21.303	6.88	>13
30	53.1	95.58	8.767	18.768	6.95	>13
60	53.1	191.16	7.708	17.375	7.02	>13
90	53.1	286.74	7.254	16.269	6.98	>13
120	53.1	382.32	6.418	15.607	7.08	>13

Fumasep FBM-PK

time / min	|Current| / mA	Charge / C	R cathode-reference	R cathode-anode	pH catholyte	pH anolyte
0	0	0	9.984	18.925	6.83	>13
30	53.1	95.58	9.248	18.272	6.84	>13
60	53.1	191.16	8.791	17.429	6.85	>13
90	53.1	286.74	8.411	17.312	6.88	>13
120	53.1	382.32	8.714	18.217	6.89	>13

Figure S3. *Chronopotentiometry analysis at 10 mA cm^{-2} for the N324 Nafion reinforced membrane and the bipolar Fumasep FBM-PK membrane.*

Thus, we tested the two membranes in CO_2 reduction process using the compact lab-scale cell to evaluate their performances and influence on the electrocatalytic activity. Figure S4 shows the FE plots for tests carried out by applying –1.0 V (vs. RHE) at the cathode.

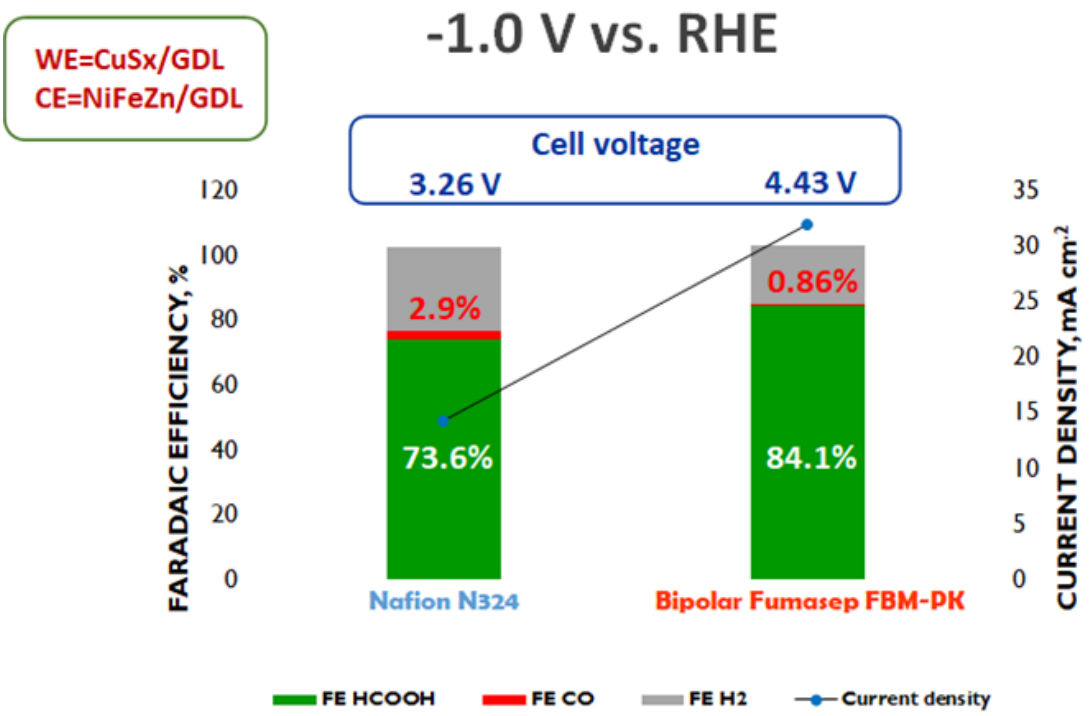

Figure S4. *Faradaic Efficiency (FE) for tests of CO_2 reduction using the N324 Nafion reinforced membrane and the bipolar Fumasep FBM-PK membrane at –1.0 V (vs. RHE).*

The working electrode was Cu-S/GDL, while the counter-electrode for water oxidation was NiFeZn/GDL. For the reinforced Nafion membrane, the FE to formic acid was 73.6% (almost 3% to CO formation), while for the bipolar membrane, the FE to formic acid was higher (84.1%). However, the cell voltage was significantly higher for the bipolar membrane configuration (4.43 V vs 3.26 V for the reinforced Nafion membrane). Thus, we chose the N324 Nafion reinforced membrane for the artificial leaf.

S4. Study of electrical losses on the compact flow electrochemical cell

Electrochemical Impedance Spectroscopy (EIS) measurements were performed in a two-compartment H-type cell in a three-electrode configuration to evaluate the resistive losses associated with each specific component of the device. We used Pt wires as working (W) and counter (C) electrodes at the anode and cathode side, respectively. Furthermore, the position of the

Ag/AgCl reference electrode was changed (near the working electrode, *configuration 1*, and near the counter electrode, *configuration 2*) to determine the resistance of the electrolyte and membrane. The series resistances measured under the two different configurations were subtracted ($R_{component} = R_{S2} - R_{S1}$) to calculate the associated resistance of a specific component (electrolyte, membrane, etc.). This method allowed us to estimate the resistance of the different membranes under study, as shown in Figure S5.

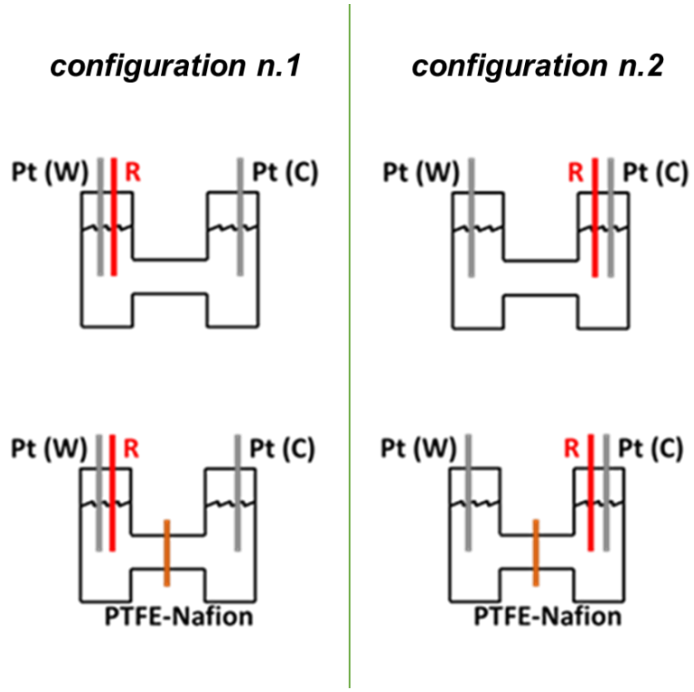

Figure S5. *Configurations 1 and 2 to determine the associated resistance to the different components in-between the two compartments of an H-type cell.*

Additionally, the exact distance between the W and C electrodes was measured as 5 cm to calculate the electrolyte resistance per length unit. The obtained values for the different components under study are summarised in **Table S2**.

Table S2. Series resistances were measured in configurations 1 and 2 to determine the resistance of each specific device element.

Component	**R_s (configuration 1)/ Ω**	**R_s (configuration 2)/ Ω**	**$R_{component}$/ Ω**
Electrolyte (0.1M $KHCO_3$)	22.5	252.5	230
Nafion N324 membrane	25.5	286.7	261.2
GDL+Nafion N324 membrane	26.9	291.3	264.4
Ni foam (as W)	16.0	270.6	254.6
GDL (as W)	25.2	268.3	243.1

From these experiments, the resistance of the 0.1M $KHCO_3$ electrolyte (46 Ω/cm), Nafion^{TM} N324, Teflon™ Fabric reinforced membrane (31 Ω), gas diffusion layer, GDL (3 Ω), and Ni foam (25 Ω), were determined. The primary electrical loss stems from the electrolyte. The distance between the anode and cathode was minimised in the design of the final proof-of-concept device to minimise this loss. GDL was also selected as the anodic support for its lower resistance than Ni foam.

S5. Electrochemical characterisation of Ni-Fe-Zn oxide

5.1 Electrode preparation on Ni-RDE for AST tests

Catalyst inks were prepared following the recipe: The catalyst (10 mg) was mixed with a 10wt% of ionomer (FAA-3 ionomer; FUMATEC), and the ink was completed with a liquid CH_3CH_2OH:H_2O mixture (3:1 in volume) to a final volume of 1 mL. The electrode substrates were cleaned in acetone and Milli-Q water before the ink deposition. Then, 84 μL of ink was drop-casted on a Nickel Rotating Disk Electrode (Ni–RDE) electrode. The electrodes were dried at 60 °C to obtain a total loading of 0.84 mg catalyst cm^{-2}. Blank electrodes were prepared following the same procedure without any catalyst content in the ink formulation.

5.2 Electrochemical characterisation

Ni-Fe-Zn oxide was supported using the FAA-3 ionomer from FUMATEC to improve the stability of the electrode. The deposition was performed by thermal spray coating. Figure S6 shows the schematic diagram of the Accelerated Stability Test (AST) protocol adopted to evaluate its stability. In contrast, Figures S7 and S8 report the experimental results of the long-term stability tests in bicarbonate media (0.1 and 1 M, respectively). The anode side was tested in a carbonate electrolyte (the same used in the cathode side) to have a single electrolyte in both cell compartments. However, Ni-Fe-Zn oxide showed low performance and some random activities in carbonate media due to the ionomer deactivation [1, 2]. We also noticed a redox peak in the overpotential range of 160-170 mV, luckily due to some areas of the Ni-RDE electrode exposed to the solution after detachment of the catalyst. The overpotential during 50 hours did not show variations to deliver 10 mA/cm^2, and the catalytic performance is higher than the values obtained in the RDE equipment (Figure S9). The main reason is the low mass transfer and diffusion effects of the poor agitation close to the electrode surface.

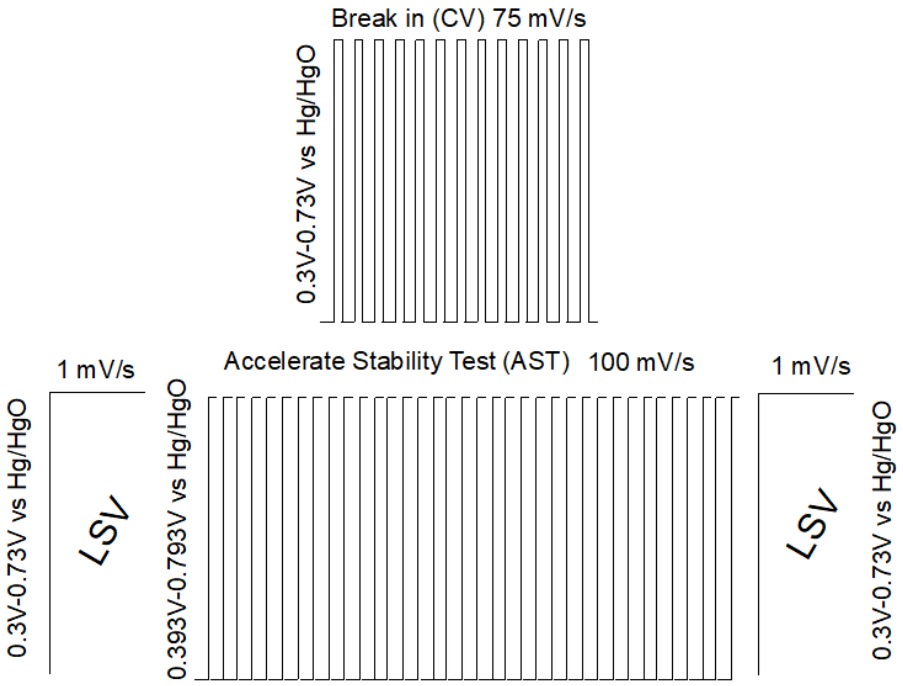

Figure S6. *Schematic diagram describing the protocol for Accelerated Stability Test (AST) performed on Ni-Fe-Zn oxide catalysts.*

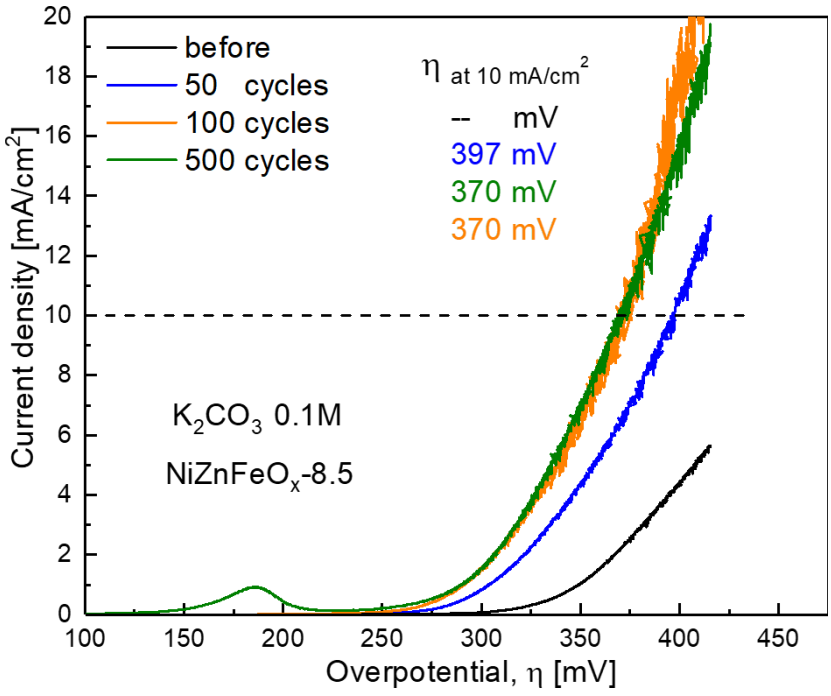

Figure S7. *Linear Sweep Voltammetry (LSV) after the Accelerated Stability Test performed for the the Ni-Zn-Fe oxide in bicarbonate media (0.1 M).*

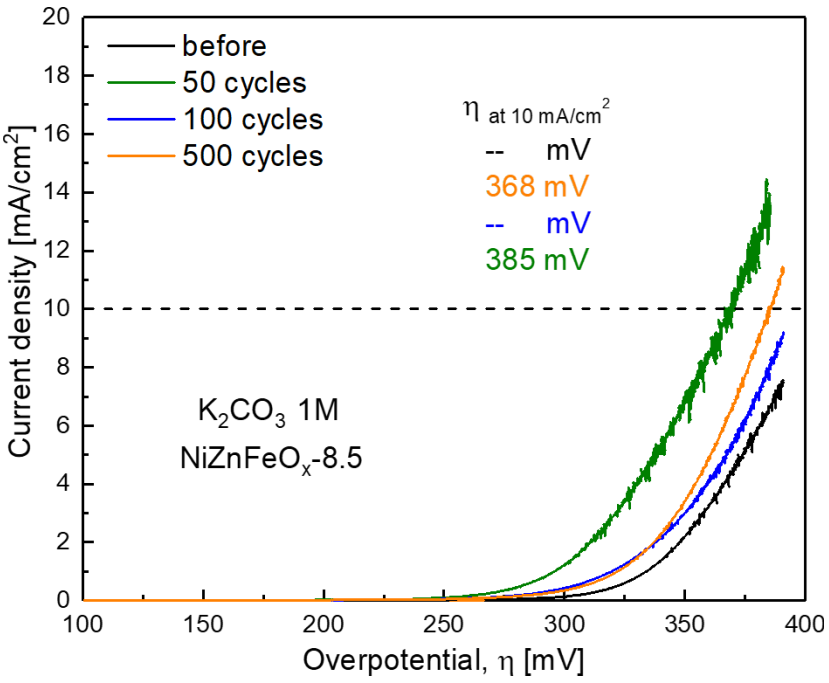

Figure S8. *Linear Sweep Voltammetry (LSV) after the Accelerated Stability Test performed for the Ni-Zn-Fe oxide in bicarbonate media (1 M).*

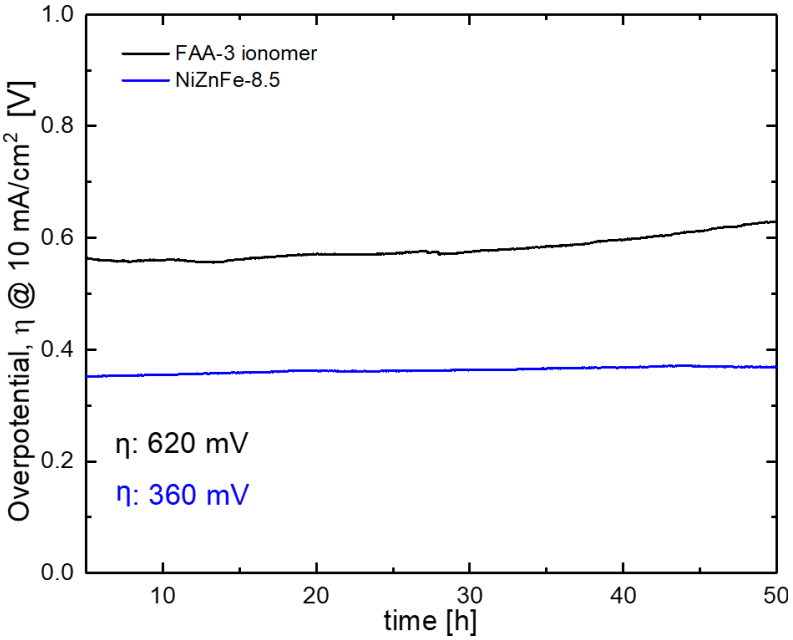

Figure S9. *Overpotential to deliver 10 mA/cm^2, showing no variations of the catalytic performance in 50 hours.*

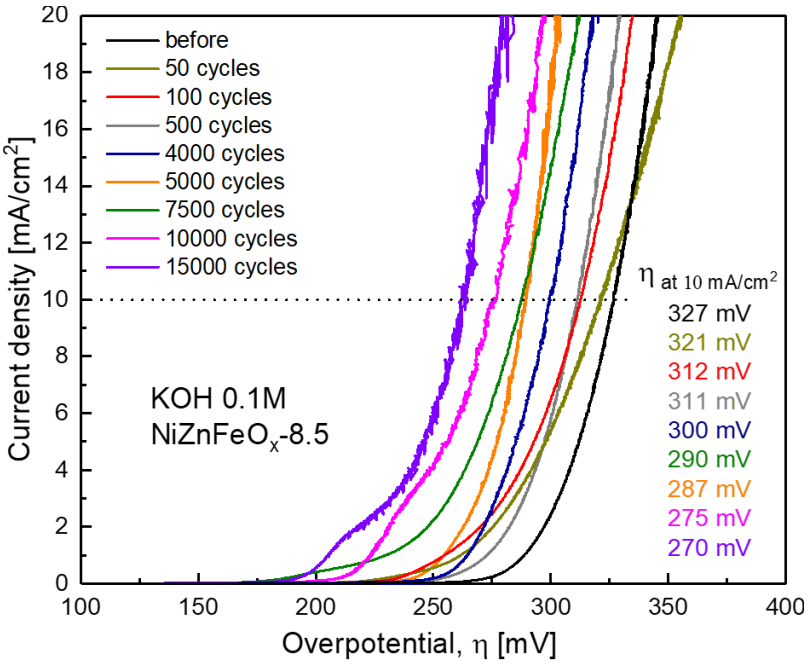

Figure S10. *Linear Sweep Voltammetry (LSV) after the Accelerated Stability Test performed for the Ni-Zn-Fe oxide in KOH 0.1M.*

On the other hand, Ni-Fe-Zn oxide electrode provided great performance in oxygen evolution reaction (OER) and exceptional stability in 0.1 M KOH. A current density of 10 mA cm^{-2} for a working electrode overpotential of 270 mV was reached for the anode after 15k cycles of harsh stability stress (see Figure S10). The catalytic performance of the Ni-Fe-Zn oxide catalyst even improved with increasing number of cycles in the AST. This behaviour during OER under carbonate-free alkaline electrolytes was due to the growth of the electrochemically-active surface area for surface re-organisation (including some initial Zn from the surface), leading to the generation of new active sites that were previously covered in some interstitial positions [3, 4]. Ion leaching increased the surface area, facilitating the accessibility of active sites to water molecules, as also commonly reported for different oxides [5]. Table S3 reports the metal leaching in the electrolyte solution after 24-hour electrocatalysis at 10 mA cm^{-2} with Ni-Fe-Zn oxide as the anode, detected by Inductively coupled plasma (ICP) technique.

***Table S3**. Leaching detected by ICP technique in the electrolyte solution after 24 hours of electrocatalytic test at 10 mA cm^{-2} with Ni-Fe-Zn oxide.*

Ni Leaching	Zn leaching	Fe leaching
< 0.2 %	8.2 %	< 0.2 %

Figure S11 shows images of the as-prepared Ni-Fe-Zn oxide obtained by Scanning Transmission Electron Microscopy (STEM) in the high-angle annular dark field (HAADF) and High-Resolution Transmission Electron Microscopy (HRTEM). The features are identical to those obtained for the analysis of the post-electrolysis sample (which are reported in the main text on Figures 2c,d,e). evidencing the high robustness of the bulk material.

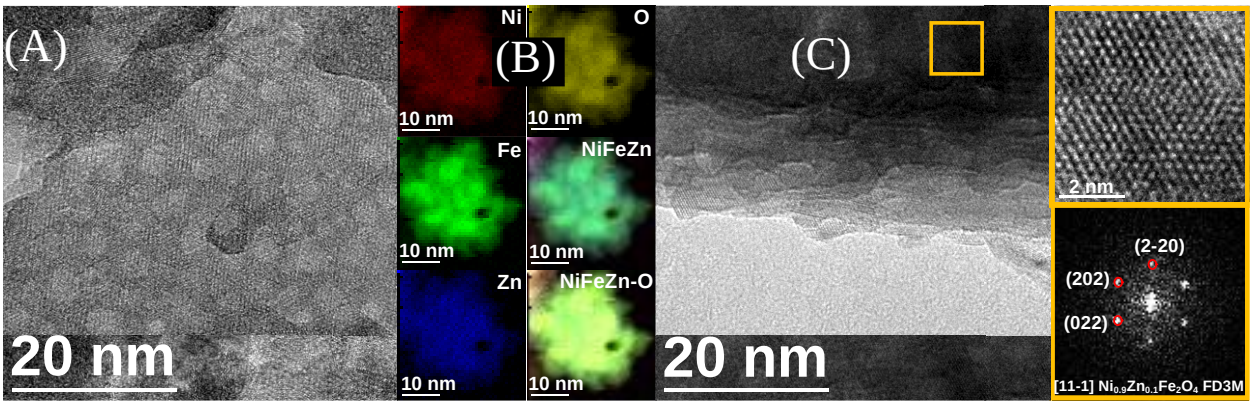

***Figure S11.** As-prepared Ni-Fe-Zn oxide: A) HAADF STEM micrograph of Ni-Fe-Zn nanoblock sample; B) EELS chemical composition maps obtained of the STEM micrograph, showing individual Ni L2,3-edges at 855 eV (red), Fe L2,3-edges at 708 eV (green), Zn L2,3-edges at 1020 eV (blue) and O K-edge at 532 eV (yellow) as well as composites of NiFeZn and NiFeZn-O; c) High-Resolution Transmission Electron Microscopy (HRTEM) image taken from an agglomerate nanoparticle squared in orange. Detail of the orange squared region and its corresponding power spectrum reveals that this nanoparticle has a crystal phase in agreement with the $Ni_{0.9}Zn_{0.1}Fe_2O_4$ cubic phase (space group = FD3M) with a=b=c=8.3540 Å. From the crystalline domain in the inset, the $Ni0.9Zn0.1Fe_2O_4$ lattice fringe distances are measured to be 0.294 nm, 0.292 nm and 0.295 nm, at 60.64° and 121.06°, which could be interpreted as the cubic $Ni_{0.9}Zn_{0.1}Fe_2O_4$ phase, visualised along its [11-1] zone axis.*

S6. Protocol for electrochemical reduction tests

The electrochemical tests were performed by following a defined order of operations. After measuring the open circuit voltage (OCP), preliminary cyclic voltammetry (CV) analysis was performed to stabilise the electrocatalyst from +0.2 V (vs. RHE) to the set potential, then used for the chronoamperometry (CA) test (scan voltage rate = 20 mV s^{-1}). Many CV cycles were necessary to reach stable behaviour. Once the system reached a steady state after about 20-30 cycles, the CV analysis was stopped. After some minutes needed to stabilise and to measure the OCP again, the double-layer technique was used to evaluate the capacitance. This method consists of an additional set of CV cycles performed at an increasing voltage rate (from 2 up to 50 mV s^{-1}) but in a narrow range of voltage centred around the OCP (± 0.016 V). The values of current density obtained for each voltage (two points, one for positive and one for negative voltage scan rates) were then plotted (Y-axis) against the voltage scan rate (X-axis), as reported in Figure S12.

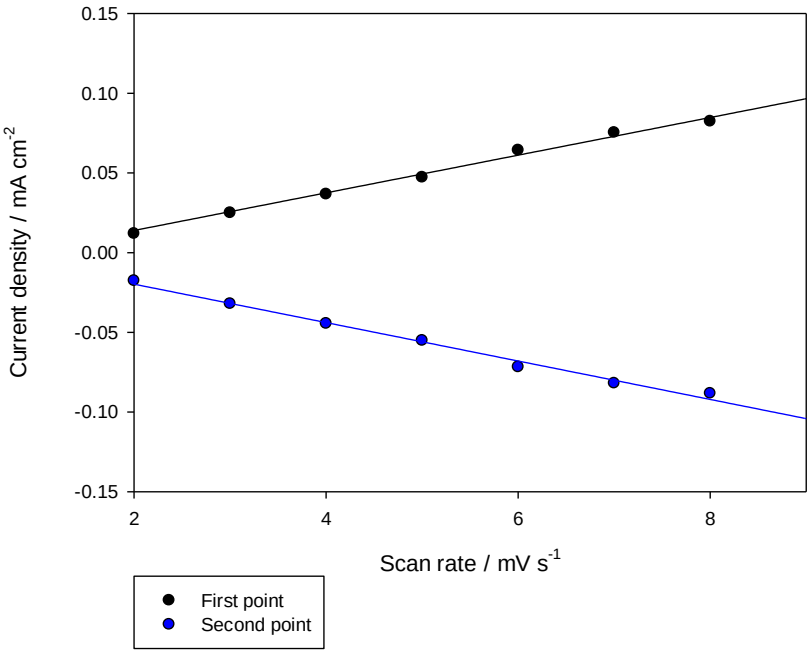

Figure S12. *Example of double layer plot for capacitance estimation.*

The two straight-line slopes (in absolute value) obtained from the linear regression profiles were averaged and used as the capacitance (in μF cm^{-2}).

After these preliminary CV tests (CVs for electrocatalyst stabilisation and capacitance calculation), a 1.5 h CA test was made. The potentials investigated were -0.4, -0.6, -0.8 and -1.0 V.

Typically, the same catalyst was tested starting from the lowest voltage (-0.4 V) and finishing to the highest voltage (-0.8 V), but changing the electrolyte and washing the system after each set voltage, and adopting the whole protocol (pre-CVs, CA and post- CVs) for each set voltage. During the CA tests, both gas and liquid products were analysed. The gas products were analysed by Gas chromatography, as reported in the experimental part, sampling the outlet gas stream at a constant time interval (10 min). In contrast, the liquid products were collected in the catholyte and analysed by GC-IC at the end of the CA. The same CV analysis cycles were then repeated after the CA test.

S7. Characterisation of Cu-S electrodes (fresh and used)

7.1 X-Ray diffraction (XRD)

The XRD of Cu-S is reported in Figure S13. Notably, the graph compares the fresh Cu-S (in the form of a powder, black line) and the Cu-S deposited on the GDL after consecutive tests at -0.6, -0.8 and -1.0 V vs RHE (blue line). For the fresh Cu-S catalyst, peaks at 29.82°, 36.82°, 42.57°, 61,62° were detected, corresponding to the (110), (111), (200), (220) crystallographic planes of pure Cu_2O, respectively. However, after the chronoamperometric tests, the presence of Cu(0) was also observed, with a peak at 43.57° corresponding to the (111) plane, together with the peaks corresponding to (200) and (220) planes of Cu_2O. The plot also shows pictures of the final Cu-S electrodes after tests at different pHs.

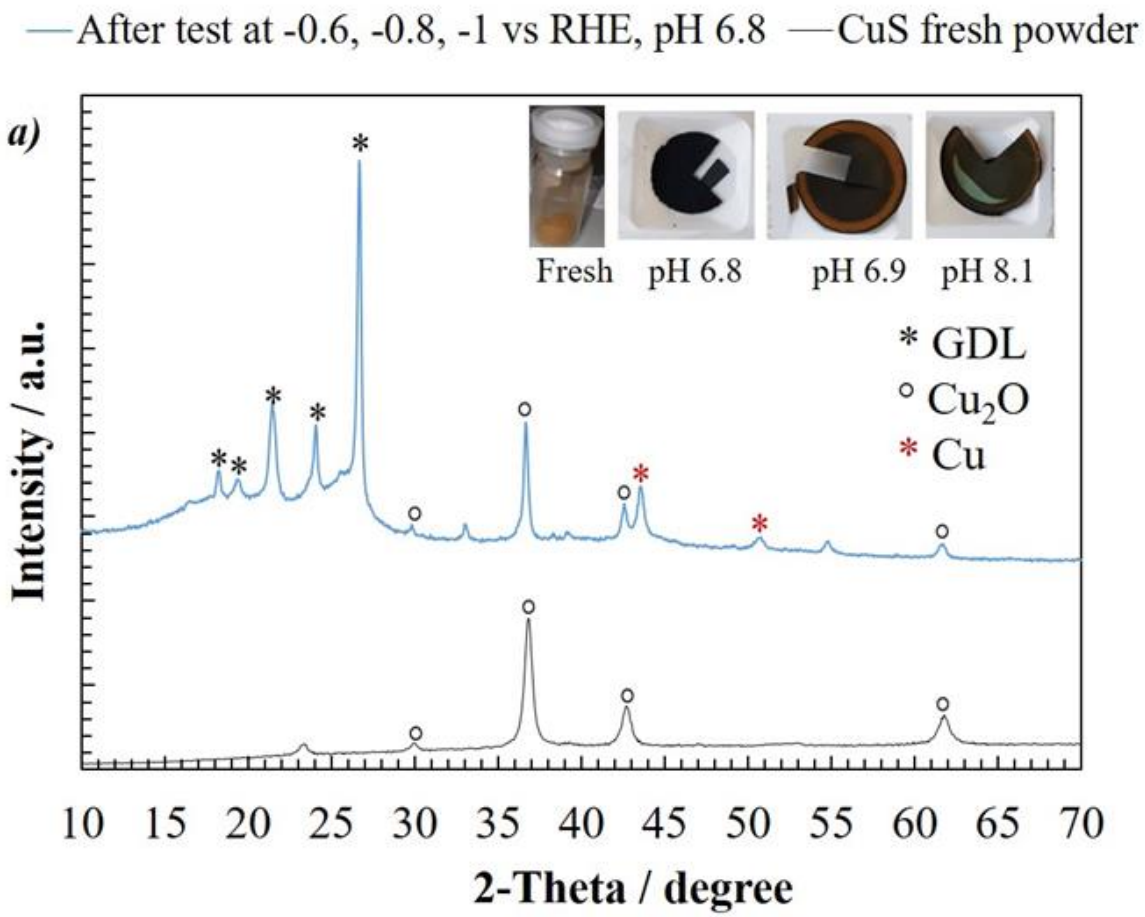

Figure S13. XRD analysis comparison of fresh and used Cu-S electrodes.

7.2 Capacitance evaluation at different potentials

Figure S14 shows the variation of the capacitance (in µF cm^{-2}), estimated with the double layer technique (as described above in section 6), before (green bar) and after the chrono-amperometry -CA- (blue bar) for each applied potential for tests with Cu-S as the cathode and bare GDL as the anode.

The initial capacitance resulted as 2687 µF cm^{-2}. Then, the data show a general decrement trend with the applied potential. Specifically, until –0.6 V vs RHE the capacitance measured after the CA remains lower than the initial value; however, this trend reverses from -0.8 V up to -1.0 V vs RHE. The lowest capacitance is 1793 µF cm^{-2}, measured before applying –0.8 V vs RHE.

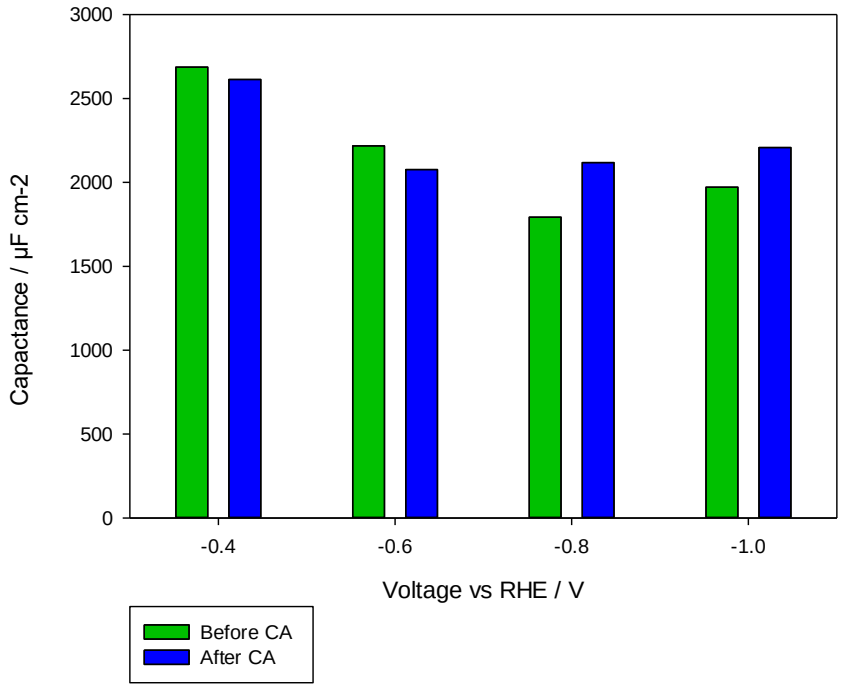

Figure S14. *Capacitance evaluated before and after the CA performed at different applied potential, with Cu-S as working electrode.*

S8 Influence of Sulfur doping

Figure S15 shows the difference in Faradaic Efficiency and current density of the behaviour of the Cu-S electrode compared with a non-doped Cu_2O electrode (without S). The introduction of sulfur increased the formation of carbon products (formate and carbon monoxide) to H_2 (produced by proton reduction), and it highly favoured the selective production of formate over CO.

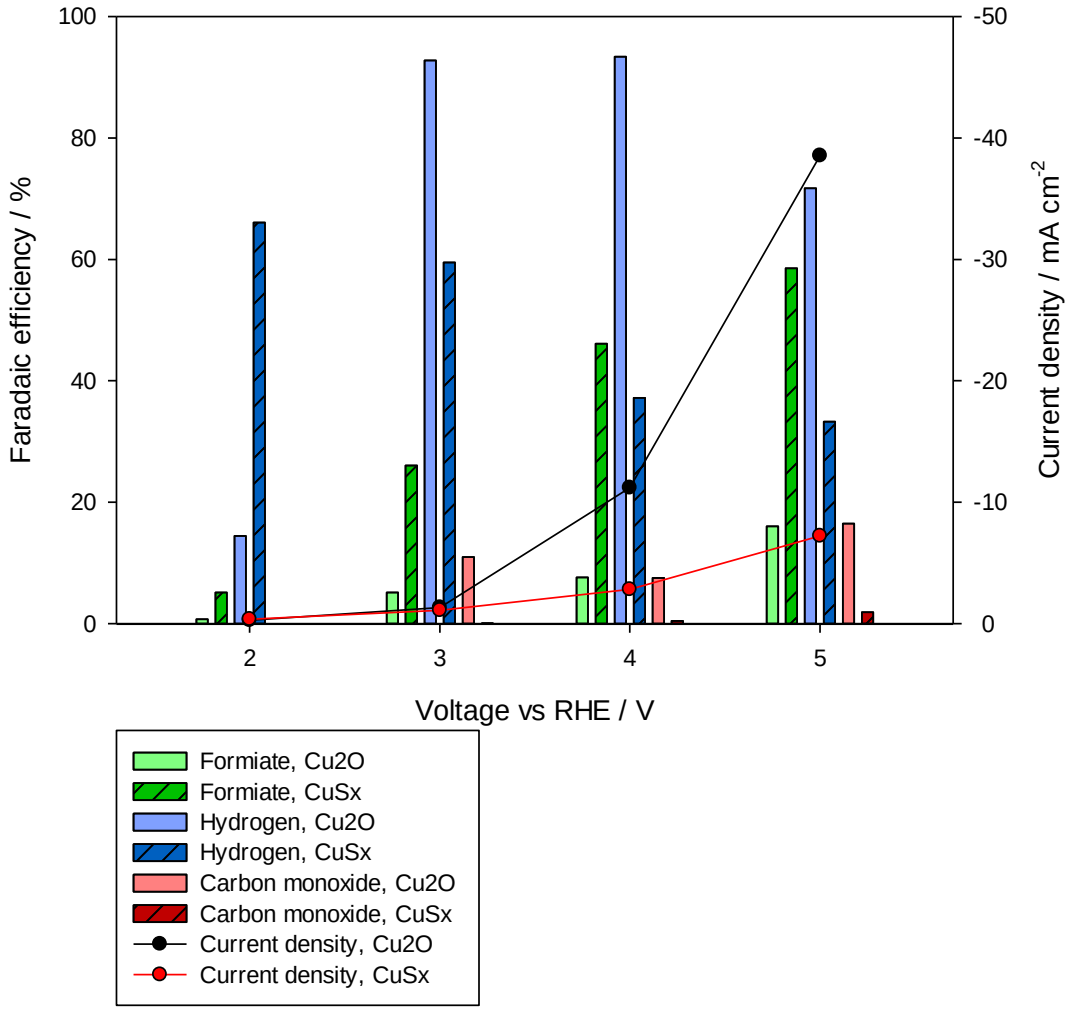

Figure S15. *Faradaic efficiency and current density for tests carried out with bare Cu_2O and Cu-S catalysts.*

S9. IV characteristics of the PV module

Figure S16 shows the current-voltage (IV) characteristics and the photovoltaic (PV) parameters of the 4-cell Silicon heterojunction (SHJ) module with shingled interconnection, measured in Jülich under standard test conditions (illumination intensity of 100 mW cm^{-2} with an AM1.5G spectrum at T = 25 °C) by using Wacom Solar Simulator WXS-140S-Super. Under these conditions, the PV module provides 20.3% conversion efficiency at the maximum power point (MPP) at 2.361 V.

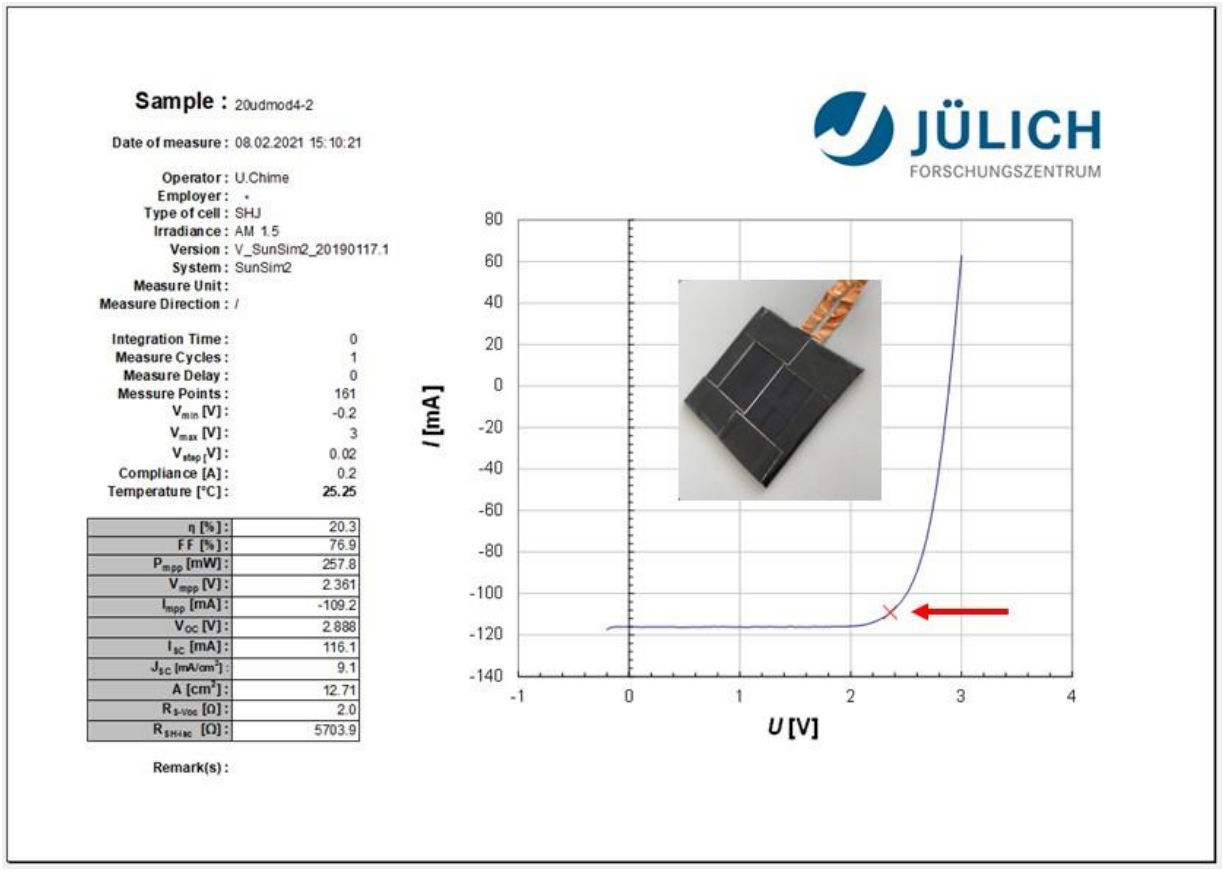

Figure S16. *IV characteristics and photovoltaic (PV) parameters of 4-cell Silicon heterojunction (SHJ) module with shingled interconnection (area of 12.71 cm^2).*

S10. Calibration of the PV module

The 4-cell Silicon heterojunction (SHJ) module with shingled interconnection was calibrated at the University of Messina by irradiating it with a solar simulator (a Xe arc-lamp of 300 W equipped with an AM1.5G filter) to obtain the same current with respect to the polarisation curve reported in Figure S15 in the voltage range 0-2 V (constant voltage signal), i.e. 116.1 mA. This current was regulated by adjusting two variables: i) the focus of the lamp (by opening the diaphragm) and ii) the distance of the module from the lamp. A spectroradiometer system (Lot Oriel, model ILT950) was also used to measure the irradiance directly. The aim was to calibrate the system to work at 1 SUN (100 mW cm^{-2}).

Figure S17 shows the plot of current versus time at 1 V for calibrating the module at 1 SUN, and a picture of the SHJ 4-cell module irradiated by the collimated beam from the solar simulator.

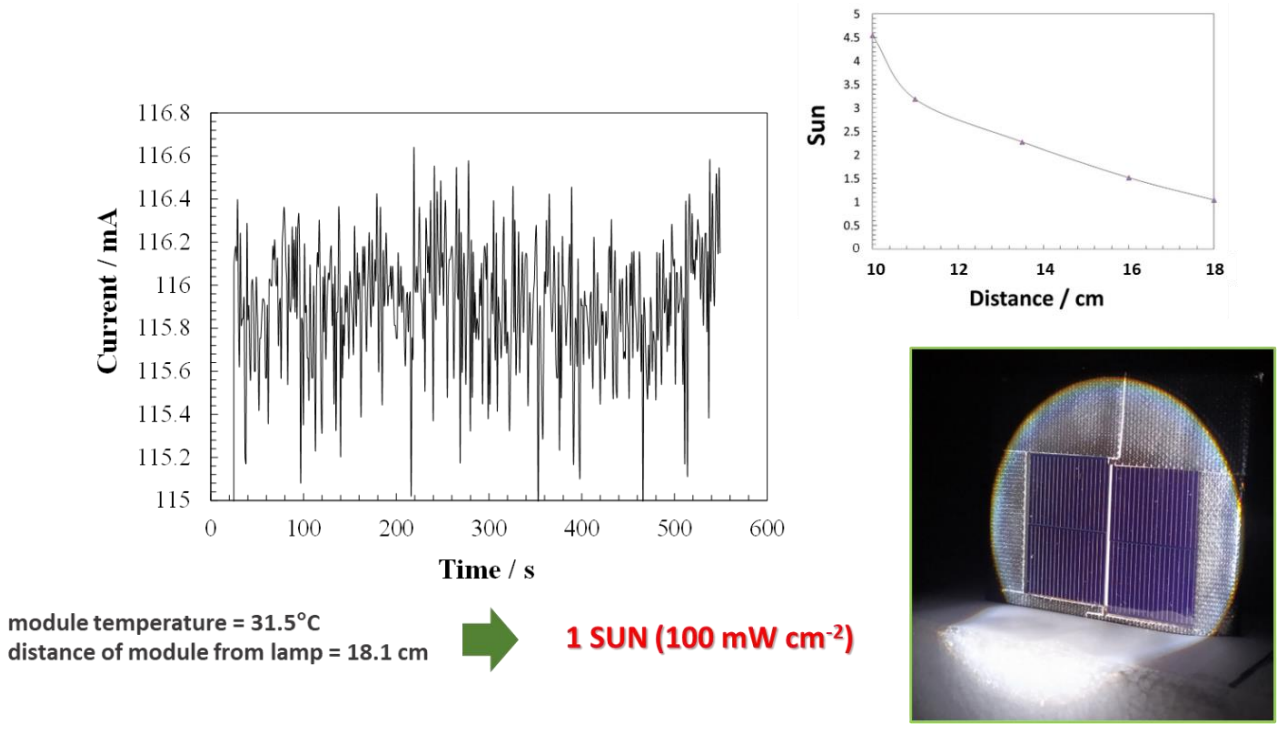

Figure S17. *Calibration of the solar simulator. A plot of current versus time at 1 V for calibrating the SHJ module at 1 SUN. A picture of the SHJ module irradiated by the collimated beam from the solar simulator is also shown.*

References

[1] J.R. Varcoe, P. Atanassov, D.R. Dekel, A.M. Herring, M.A. Hickner, P.A. Kohl, A.R. Kucernak, W.E. Mustain, K. Nijmeijer, K. Scott, T. Xu, L. Zhuang, Anion-exchange membranes in electrochemical energy systems, *Energy Environ. Sci.*, 2014, **7**, 3135−3191. doi: 10.1039/c4ee01303d

[2] J. Parrondo, C.G. Arges, M. Niedzwiecki, E.B. Anderson, K.E. Ayers, V, Ramani, Degradation of anion exchange membranes used for hydrogen production by ultrapure water electrolysis, *RSC Adv.*, 2014, **4**, 9875−9879, doi: 10.1039/c3ra46630b

[3] F.A. Garcés-Pineda, H.C. Nguyën, M. Blasco-Ahicart, M. García-Tecedor, M. de Fez Febré, P.-Y. Tang, J. Arbiol, S. Giménez, J.R. Galán-Mascarós, N. López, Push-Pull Electronic Effects in Surface-Active Sites Enhance Electrocatalytic Oxygen Evolution on Transition Metal Oxides, *ChemSusChem*, 2021, **14**, 1595–1601, doi: 10.1002/cssc.202002782

[4] H.C. Nguyën, F.A. Garcés-Pineda, M. de Fez Febré, J.R. Galán-Mascarós, N. López, Non-redox doping boosts oxygen evolution electrocatalysis on hematite, *Chem. Sci.*, 2020, **11**, 2464–2467, doi: 10.1039/c9sc05669f

[5] James B. Gerken, Sarah E. Shaner, Robert C. Mass´e, Nicholas J. Porubsky and Shannon S. Stahl, A survey of diverse earth abundant oxygen evolution electrocatalysts showing enhanced activity from Ni–Fe oxides containing a third metal, Energy Environ. Sci., 2014, 7, 2376–2382, doi: 10.1039/c4ee00436a